Journal of
Marine Science and Engineering

MDPI

Article

Influence of Remote Internal Tides on the Locally Generated Internal Tides upon the Continental Slope in the South China Sea

Zheng Guo [1], Anzhou Cao [2,3,*] and Shuya Wang [4,5]

1 Marine Science and Technology College, Zhejiang Ocean University, Zhoushan 316021, China; guozheng@zjou.edu.cn
2 Ocean College, Zhejiang University, Zhoushan 316022, China
3 Laboratory for Regional Oceanography and Numerical Modeling, Qingdao National Laboratory for Marine Science and Technology, Qingdao 266100, China
4 Key Laboratory of Physical Oceanography, Ocean University of China, Qingdao 266100, China; wangshuya@stu.ouc.edu.cn
5 Qingdao National Laboratory for Marine Science and Technology, Qingdao 266100, China
* Correspondence: caoanzhou@zju.edu.cn

Abstract: In this paper, the M_2 internal tides (ITs) originating from the continental slope in the South China Sea are studied using the CROCO model. The simulation results show that there are two origins of ITs on the continental slope: at 118°–119.5° E along 22° N near the southern entrance of the Taiwan Strait and at 117°–118° E along 20° N near Dongsha Island. The local generation of ITs is greatly influenced by the ITs that radiate from the Luzon Strait (LS). The integrated conversion at the first generation site is increased by 31% to 0.42 GW compared to the case where the LS is excluded from the simulation region. Its maximum energy flux almost doubles to 2.5 kW/m, which is 10% of the westward component. The existence of the other IT beams from Dongsha Island is attributed to the ITs from the LS. The local generation on the continental slope changes when remotely generated ITs alter the amplitudes and phases of the bottom pressure perturbation. These results indicate that the ITs originating from the LS contribute to the spatial variation of ITs in the SCS by modulating the IT generation on the continental slope.

Keywords: internal tides; South China Sea; continental slope; numerical simulation

Citation: Guo, Z.; Cao, A.; Wang, S. Influence of Remote Internal Tides on the Locally Generated Internal Tides upon the Continental Slope in the South China Sea. *J. Mar. Sci. Eng.* **2021**, *9*, 1268. https://doi.org/10.3390/jmse9111268

Academic Editor: Edward J. Anthony

Received: 9 October 2021
Accepted: 10 November 2021
Published: 15 November 2021

1. Introduction

The internal tide (IT) is an important intermediate step of the tides-to-turbulence cascade, which connects large- and small-scale motions. It plays an important role in the dissipation of surface tidal energy and the enhancement of mixing. The ITs in the South China Sea (SCS) are fairly intense. The complete evolution of ITs in the SCS has been investigated widely through in situ observation [1–3], satellite altimeter data [4,5], and numerical model simulations [6–8]. However, ITs locally generated in the SCS have long been ignored. The authors of [9] revealed a number of generation sites in the simulation of the M_2 ITs in the Western Pacific, including the southern Taiwan Strait, which was confirmed in later studies [8,10,11], yet the ITs generated at the LS were so intense that they attracted the most attention and obscured weaker ITs generated at other sites.

A missing piece of evidence from the picture of the IT field in the northeastern SCS was recently retrieved by [12]. The results, which were based on 26-year altimeter data, revealed a southward M_2 IT beam and a much weaker eastward beam originating from the continental slope. The southward M_2 beam starts from the southern Taiwan Strait and propagates for about 300 km. Its integrated flux is 0.18 GW, or approximately 10% of the westward LS flux. The beam is sufficiently intense to interfere with the westward flux, forming a multiwave IT field featuring significant spatial variations.

The ITs from the continental slope deserve more investigation because of their complexity under the influence of remote ITs. By altering bottom pressure perturbations on the continental slope, remote ITs can modulate the local generation of ITs considerably, resulting in the intermittency of ITs on the continental slope [13]. This has been further verified by oceanic observations and numerical modelling [14,15]. Given that the continental slope in the SCS is also under the pathway of ITs from the LS, we aim to analyze their contribution to the local generation on the continental slope in the northern SCS in this study.

The rest of the paper is arranged as follows. Section 2 introduces the model settings and analysis method. In Section 3, the model simulation is first validated and the influence of the ITs from LS on the local generation on the continental slope is examined. Finally, the findings of this paper are summarized in Section 4.

2. Methodology

2.1. Model Configuration

This study employs the Coastal and Regional Ocean COmmunity (CROCO) model (version 1.0; https://www.croco-ocean.org, accessed on 10 November 2017) which is built based on the regional ocean modelling system from Institut de Recherche pour le Developpement (ROMS_AGRIF). The model solves the original governing equations under the Boussinesq approximation and hydrostatic equilibrium. The model performs well in different scenarios [16–18]. The use of hydrostatic approximation is still valid for this study, taking into consideration the fact that in the northern SCS the M_2 ITs wavelength is much larger than the water depth [5,8] and the non-hydrostatic processes are beyond our scope.

The domain of the simulation is shown in Figure 1a. The model has a uniform horizontal resolution of 1/20° and 25 uneven sigma vertical layers, with a thicker distribution near the bottom and surface. The Large–McWilliams–Doney k-profile parameterization mixing scheme [19] is used for the vertical turbulent mixing of momentum and tracers. The Laplacian horizontal mixing of momentum is used for the subgrid-scale turbulence. The realistic topography extracted from 1 min gridded elevations/bathymetry for the world (ETOPO1) data [20] is used in the simulation. The topography has been smoothed to reduce the horizontal pressure gradient errors. The stratification is set to be horizontally homogenous by spatially averaging the salinity and temperature extracted from the World Ocean Atlas 2009 (WOA09) (Figure 1). The model is forced at four open boundaries with the M_2 tide. Its barotropic currents and surface elevations are extracted from the Oregon State University Ocean Topography Experiment TOPEX/Poseidon Global Inverse Solution (TPXO7.2; [21]). The Flather condition is used for the barotropic currents and the radiative condition is used for the baroclinic currents at the four open boundaries. A 0.5°-wide (ten cells) sponge layer is set to absorb the baroclinic energy and avoid reflection.

To investigate the mechanism underlying the M_2 tides originating from the continental slope, two cases were designed based on the CROCO model:

The Full case: the domain covers an area of 115.5°–126.5° E and 16°–26° N, including the LS, the continental slope in the northern SCS, and part of the Western Pacific.

The Slope case: the longitudes of the domain range from 115.5° E to 120° E. In this case, the LS, the most important IT generation site, is excluded. Therefore, we can investigate the influence of ITs originating from LS on the continental slope by comparing the results gained with the results of the Full case.

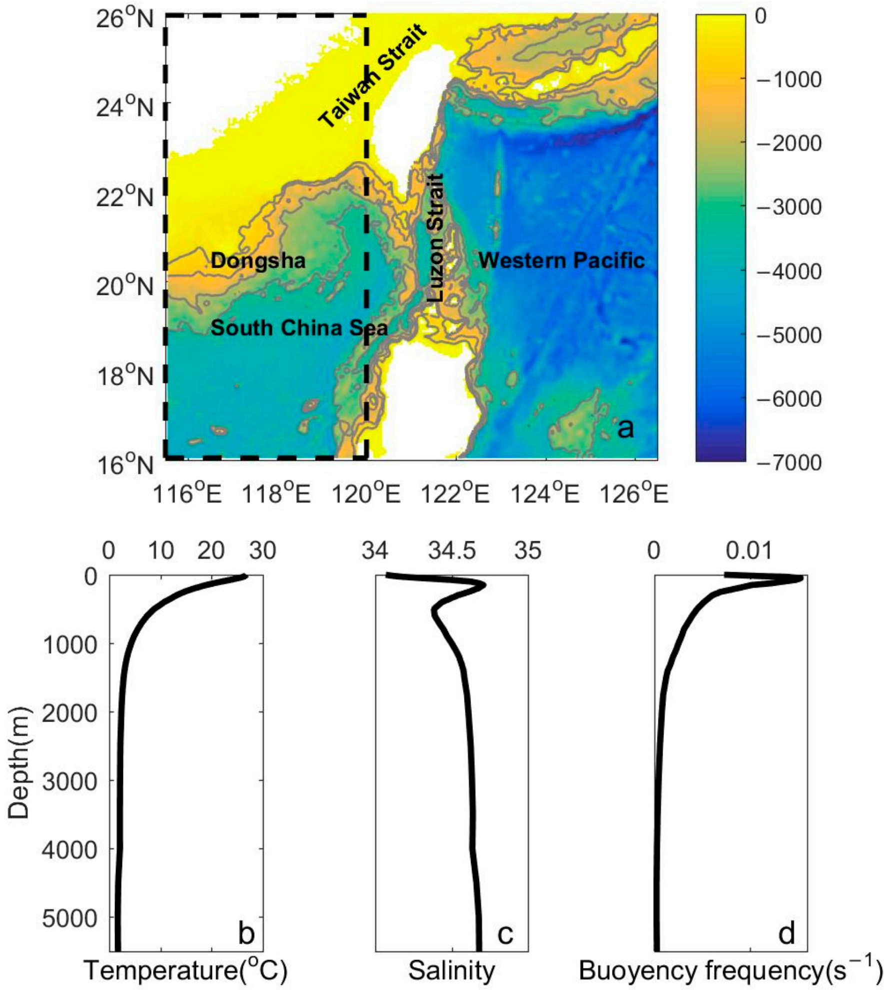

Figure 1. (**a**) Depth in the northern SCS (shading, unit: m). Gray lines indicate isobathic contours of −3000, −2000, −1000, and −500 m. The dashed rectangle denotes the simulation area for the Slope case. Initial (**b**) temperature, (**c**) salinity, and (**d**) buoyancy frequency profiles in the model.

2.2. Baroclinic Energy Equation

The depth-integrated baroclinic energy flux F_{bc} is calculated as follows [22,23]:

$$F_{\mathrm{bc}} = \int_{-H}^{\eta} p'(z,t)u'(z,t)dz \tag{1}$$

where η is the sea surface elevation, H is the water depth, p' is the pressure perturbation, and u' is the horizontal baroclinic velocity. The pressure perturbation is calculated as follows [24]:

$$p'(z,t) = p_{surf}(t) + \int_{z}^{\eta} \rho'(\widehat{z},t)g d\widehat{z} \tag{2}$$

where z is the depth of p', ρ' is the density perturbation, g is the acceleration due to gravity, and p_{surf} is the surface pressure, which can be solved by:

$$\frac{1}{H+\eta}\int_{-H}^{\eta} p'(z,t)dz = 0 \tag{3}$$

The horizontal baroclinic velocity is:

$$u'(z,t) = u(z,t) - \overline{u}(z) - \overline{u}_0(t) \tag{4}$$

where u, $\overline{u}$, and $\overline{u}_0$ denote instantaneous, time-averaged, and depth-averaged horizontal velocities, respectively. The depth-averaged velocity can be obtained through:

$$\frac{1}{H+\eta}\int_{-H}^{\eta} u'(z,t)dz = 0 \tag{5}$$

The barotropic-to-baroclinic energy conversion rate E_{bt2bc} can be calculated by multiplying the pressure perturbation by the bottom vertical barotropic velocity:

$$E_{\text{bt2bc}} = p'(-H,t)w_{\text{bt}}(-H,t) \tag{6}$$

Under the assumption of incompressible water, the vertical barotropic velocity at the seafloor can be calculated as follows:

$$w_{\text{bt}}(-H,t) = u_{\text{bt}}(-H,t)\cdot\nabla(-H) \tag{7}$$

According to [25], the tidal-period-averaged conversion rate can be obtained as follows:

$$< E_{\text{bt2bc}} >= 0.5P'(-H)W_{\text{bt}}(-H)\cos(\theta_{p'} - \theta_{w_{\text{bt}}}) \tag{8}$$

where $P'(-H)$ and $W_{\text{bt}}(-H)$ are the amplitudes of the pressure perturbation and vertical barotropic velocity at the seafloor and θ_p and θ_w are their phases, respectively.

2.3. Wave Decomposition

Based on Hilbert transform [26], we decompose the IT field into components that propagate in different directions. Wave decomposition is conducted in the following steps [15]: first, take the Hilbert transform of a real-valued signal $\psi(x,y,t)$ (pressure perturbation p' or baroclinic velocity u' in our case) in time to give a spatial field of complex amplitudes for each frequency $\hat{\psi}(x,y,\omega)$; second, take the two-dimensional Fourier transform of $\hat{\psi}(x,y,\omega)$ to give $\widetilde{\psi}(k,l,\omega)$, where k and l are horizontal wavenumbers; third, define a filter function $H(k,l)$ that is equal to unity for the wavenumbers of interest and zero elsewhere; fourth, take the inverse Fourier transform of the filtered amplitude $H(k,l)\ \widetilde{\psi}(k,l,\omega)$ to give the signal in the direction of interest. The method has been successfully used in previous studies [15,27–30].

In this study, the pressure perturbation field and baroclinic velocity at each depth were decomposed into three components—the eastward (−40–90°), westward (90–240°), and southward (240–320°) components—as in [12] and used to compute the energy fluxes (Equation (1)).

3. Results

3.1. Validation of the Simulated Results

The accuracy of the simulated results was first examined before we explored the M_2 ITs originating from the continental slope. Figure 2 displays the M_2 barotropic tide extracted from the model output and TPXO7.2. The simulated amplitudes and phases of the M_2 barotropic tide are generally consistent with those from TPXO7.2 and previous studies [8,22], all of which show that the amplitudes of the M_2 tide in the SCS are slightly smaller than those in the Western Pacific but reach their maxima in the Taiwan Strait. The difference between the simulation and TPXO7.2 results in each grid was quantified as follows [31]:

$$E = \sqrt{\frac{1}{2}(A_T^2 + A_C^2) - A_T A_C \cos(G_T - G_C)} \tag{9}$$

where A and G denote the M_2 barotropic tide amplitudes and phases, respectively, and the subscripts T and C represent results from TPXO7.2 and CROCO, respectively. The domain-averaged error is 4.7 cm, confirming the accuracy of the model output. The most obvious differences between the two co-tidal charts are small-scale fluctuations superposed on the co-phase lines in Figure 2a, which are actually the modulation of ITs to barotropic tides [5,8,32].

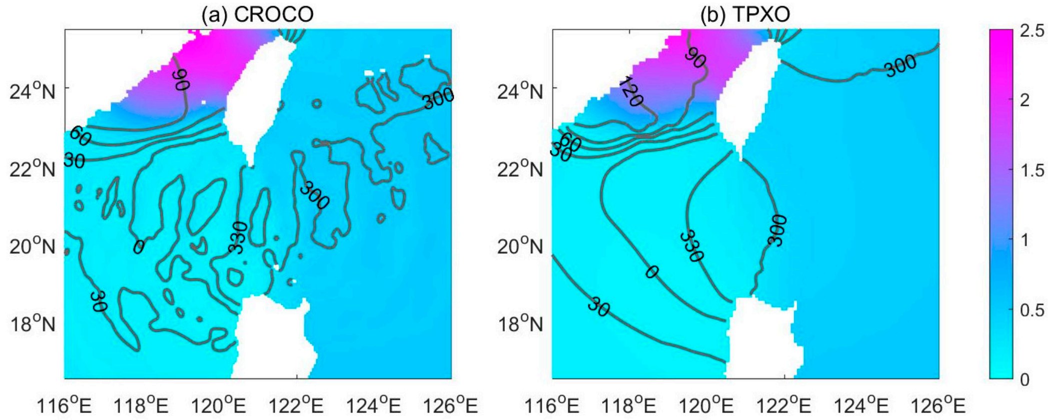

Figure 2. The M_2 surface elevations amplitudes (shading, unit: m) and phases (grey lines, unit: degrees) extracted from (**a**) the Full case simulation and (**b**) the TPXO7.2 tidal model.

To validate the compacity of the model for the IT simulation, we ran an extra case forced by the S_2 tide. The model setting was the same as that forced by the M_2 tide. The semidiurnal energy flux (M_2 + S_2) was calculated and compared with in situ observations from [33] (Figure 3). At most stations along the northern and stronger beam of the westward-propagating IT, the magnitude and direction of the model results agree well with the observations, while the simulated ITs are slightly weaker than the observations in the southern part of the LS. The deviation is probably caused by the spatially varying stratification and subtidal background currents (e.g., the mesoscale eddies and the Kuroshio) [8,22], which are not considered in this study.

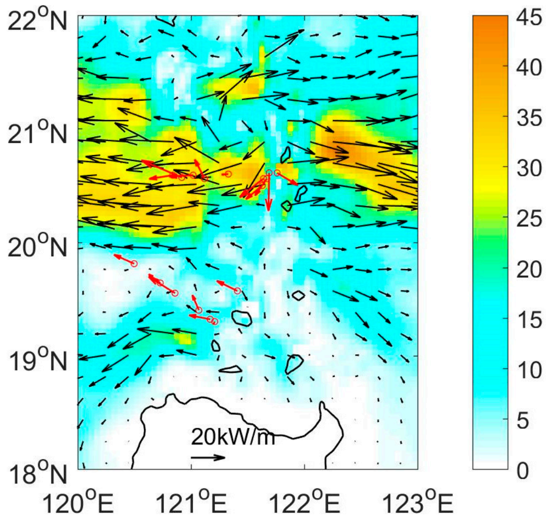

Figure 3. Simulated (black arrows) and observed (red arrows) semidiurnal energy flux at the LS. The magnitude of the energy flux is indicated by shading (unit: kW/m).

The basic characteristics of the M_2 ITs are displayed in Figure 4. The conversion rates around the LS are the largest, and there are multiple generation sites at other prominent topographic features, including the continental shelf slope in the SCS and the ridges along the Ryukyu Island chain [9,34]. The simulation results reproduce the clockwise cycle of the IT energy flux induced by a resonance mechanism in the LS, which has been investigated in previous research [7]. Departing from the LS, the M_2 IT beam propagating eastward into the Western Pacific is intense, with its maximum energy flux reaching 35 kW/m. The

ITs in the SCS bifurcated into two beams: the northern beam propagating westward to the Dongsha Island is of comparable intensity to the eastward beam, while the southern beam propagating southwest is much weaker. The results are consistent with satellites observations [5] and previous numerical simulations [8–10].

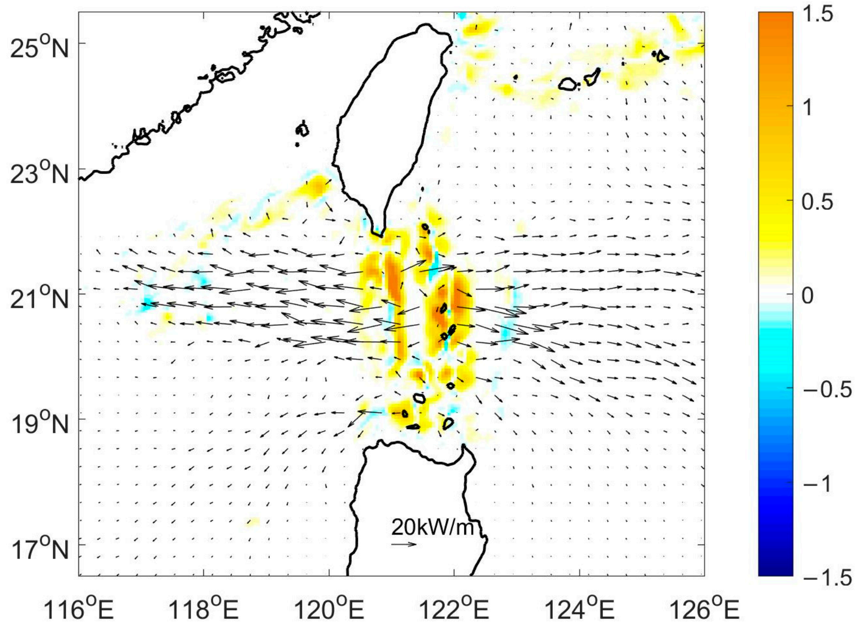

Figure 4. The M_2 baratropic-to-baroclinic conversion rates (shading, unit: W/m^2) and the ITs depth-integrated baroclinic energy fluxes (quiver) in the simulation domain.

3.2. ITs Originating from the SCS Continental Slope

We applied Hilbert transform to the wave field to obtain three components of the M_2 tides: westward (90–240°), southward (240–320°), and eastward components (−40–90°). The first two components are displayed in Figure 5, while the eastward component is too weak and therefore not discussed here. The westward component has a comparable magnitude to the multidirectional ITs field shown in Figure 4, implying its dominant role. The two westward beams have been reported in many previous studies [5], and in the following we focus on the southward component. This component propagates in a south-southeast direction from two origins: 118–119.5° along 22° N and 117–118° along 20° (Figure 5c). The former branch is stronger, with a maximum energy flux of 2.5 kW/m, but it is only approximately 10% of the westward component in terms of intensity, which is consistent with the findings of [12]. Recalling the findings in [12], we can also see a few differences: first, our simulation results show two south-southeast beams, while the satellite results in [12] reveal a southward component and an eastward component originating from the continental slope; second, the simulated ITs are stronger than the satellite observation. The underestimation of energy flux by altimeter has been pointed out in previous studies [5]; the difference in direction may be due to the subtidal circulation lacking in our simulation [22].

To further illustrate the ITs field, we select two sections along the ITs propagation paths and display snapshots of the zonal current of the westward component (116° E–119.5° E, 21° N) and the meridional current of the southward component (119° E, 17° N–23° N) at the end of the simulation (Figure 6). The directions of the velocities of the westward component are different in the upper and lower layers, indicating the dominance of mode 1. The southward component is less energetic than the westward component, and shows the characteristic of higher modes: the baroclinic velocity changes its direction two or more times. The multimodal structure of the southward component may be related to local generation, which will be shown in the following section.

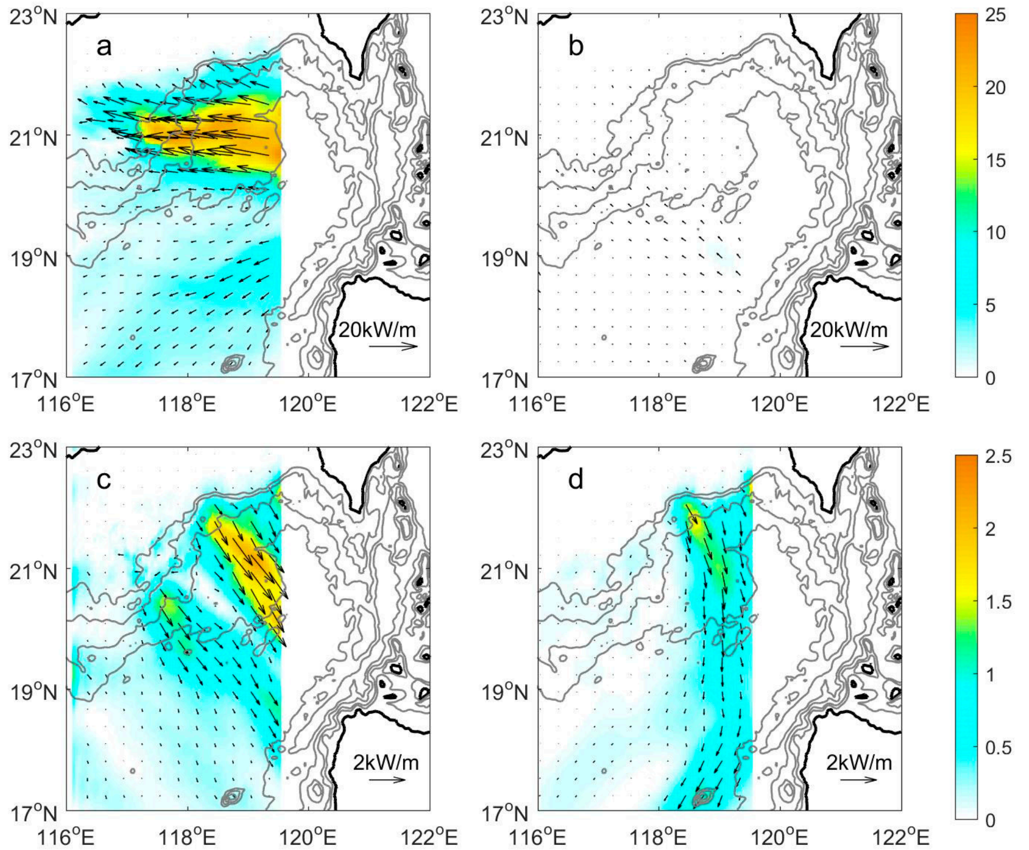

Figure 5. Depth integrated energy flux of the (**a**,**b**) westward, and (**c**,**d**) southward components in (**a**,**c**) the Full case and (**b**,**c**) the Slope case. The shadings indicate the magnitude (unit: kW/m) and the arrows show the directions. The gray lines indicate isobathic contours of −3000, −2000, −1000, and −500 m.

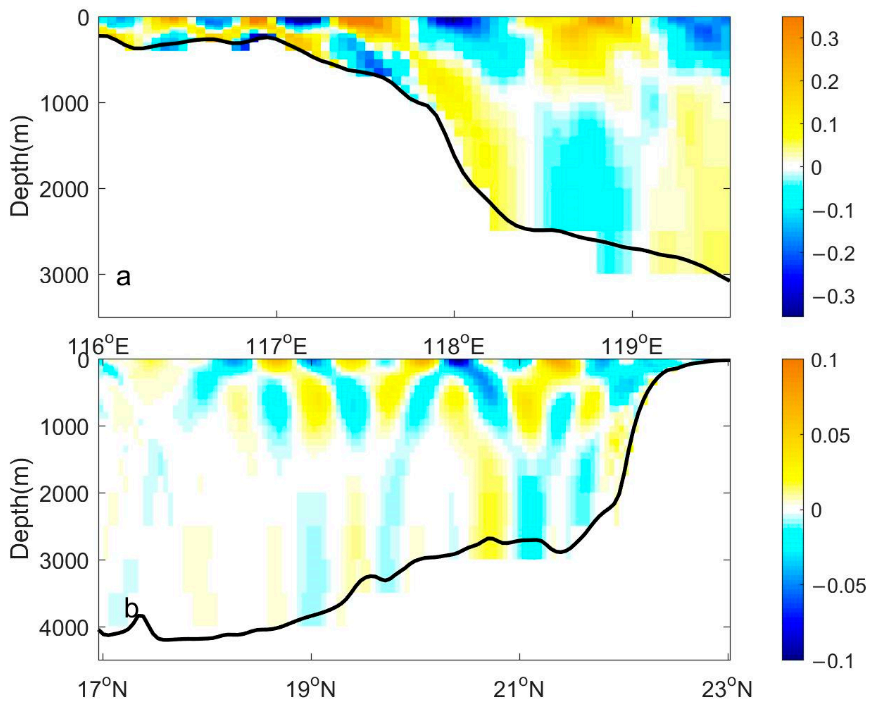

Figure 6. Snapshots of (**a**) the zonal baroclinic currents along 21° N and (**b**) the meridional baroclinic currents along 119° E (shading, unit: m/s) at the end of the simulation.

To investigate the generation of the southward ITs, we run the Slope case where the LS is excluded while the other settings remain the same as those in the Full case. The decomposed components of the ITs fields are shown in Figure 5b,d. The west component is unsurprisingly very weak because it is generated at the double ridges in the LZ that are outside the simulation area. The southern branch of the M_2 ITs propagating southward is also missing in the Slope case, implying its close relation with the ITs that are remotely generated in the LS. Some ITs are generated between 118 and 119.5° E along 22° N, corresponding to the northern origin of the ITs southward component in the Full case. However, the magnitudes of these are much smaller and their direction is closer to due south. The results indicate that the ITs remotely generated at the LS have a major influence on those originating from the continental slope.

Figure 7a,d show the M_2 conversion rate in the two cases. The pattern of the Slope case is quite simple: only one area (118°–119.5°, 22°–22.5° N, denoted as A) shows a relatively large conversion from barotropic to baroclinic tides. The integrated conversion around region A is 0.32 GW. On the contrary, in the Full case the positive values for conversion rate alternate with negative values; in other words, the areas where ITs are generated alternate with those where energy transfers from ITs into barotropic tides. This pattern indicates the complicated influence of the remotely generated ITs. The integrated conversion around region A is 0.42 GW, up by 31% from the Slope case, although some areas within region A show a negative conversion rate. Corresponding to the southern branch of the M_2 southward component, region B (117°–118°, 20.2°–20.7° N) was identified and its integrated conversion amounts to 0.13 GW.

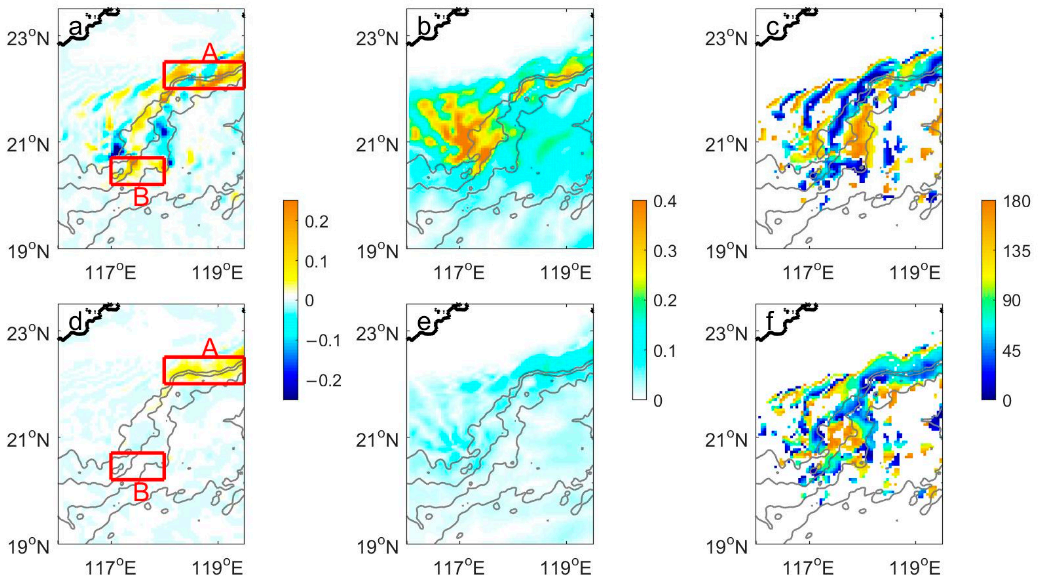

Figure 7. The M_2 tide (**a**,**d**) conversion rates (shading, unit: W/m^2), (**b**,**e**) the bottom pressure perturbation amplitudes (shading, unit: kPa), and (**c**,**f**) the phase differences between the pressure perturbation and vertical velocity at the sea floor (shading, unit: degrees) in (**a**–**c**) the Full case and (**d**–**f**) the Slope case. Only areas with a conversion greater than 0.01 W/m^2 are shown for clarity. The gray lines indicate isobathic contours of −3000, −2000, −1000, and −500 m.

According to Equation (8), the M_2 conversion rate is determined by the amplitudes of the vertical barotropic velocity and the pressure perturbation at the sea floor, as well as their phase difference. Taking into consideration the fact that the barotropic currents vary very slightly in the two cases, we focus on the amplitude of the pressure perturbation and the phase difference (Figure 7). A comparison between Figure 7b,d reveals that the amplitudes of the bottom pressure perturbation increase by several orders of magnitude around region A and Dongsha Island due to the arrival of remotely generated ITs. However, the changes in the conversion rate (Figure 7a,d) are more complicated, as the ITs originating from the

LS alter the phase of bottom pressure perturbation in addition to the amplitude. Under the influence of remote ITs, the phase of the pressure perturbation changes up to 180°, resulting in a negative conversion rate.

Based on the above analysis, we can draw the following two conclusions. First, around region A, the incoming ITs mainly increase the local generation by increasing the amplitude of the pressure perturbation. Second, regarding the ITs originating from near Dongsha Island, previous studies [12] have attributed them to reflection based on the fact that the local M_2 tide is very weak. The Slope case confirms that the local barotropic tide is not strong enough to generate ITs. However, the Full case shows that the arrival of ITs generated at the LS could significantly increase the pressure perturbation and hence the local generation.

4. Summary

Based on the CROCO, the current study explores the M_2 IT generation on the continental slope in the SCS. There are two origins of ITs on the continental slope: at 118°–119.5° E along 22° N to the southern Taiwan Strait, and at 117°–118° E along 20° N near Dongsha Island. At the first generation site, the ITs from the LS increase the integrated conversion by 31% to 0.42 GW, compared to the case where the LS is excluded from the simulation region. Its maximum energy flux almost doubles to 2.5 kW/m, which is 10% of the westward component. The existence of the other ITs originating from Dongsha Island is attributed to the ITs from the LS. The local generation on the continental slope changes when remotely generated ITs alter the amplitudes and phases of the bottom pressure perturbation. The reflection of the westward M_2 ITs on the continental slope has been noted in previous studies, and this paper reveals its contribution to local generation.

The ITs originating from the continental slope interfere with the intense westward ITs generated at the LS and hence contribute to the spatial variability of the properties of ITs in the SCS [12]. This study preliminarily explores the influence of remotely generated ITs (mainly from the LS) on local generation on the continental slope. Previous studies have noted that subtidal circulation and seasonal stratification could affect the generation and propagation of ITs from the LS. It is sensible to infer that the modulation of ITs will impact the local generation of ITs on the continental slope and further contribute to the variability of the IT field in the SCS.

Author Contributions: Investigation and original draft preparation, Z.G.; conceptualization, review and editing, S.W. and A.C. All authors have read and agreed to the published version of the manuscript.

Funding: This research was funded by the State Key Laboratory of Tropical Oceanography, South China Sea Institute of Oceanology, Chinese Academy of Sciences (Project No. LTO2108), the Laboratory for Regional Oceanography and Numerical Modeling, Qingdao National Laboratory for Marine Science and Technology (Project No. 2019A01), and the Fundamental Research Funds for the Central Universities (202061001).

Data Availability Statement: The reader can ask for all the related data from the first author (guozheng@zjou.edu.cn) and the corresponding author (caoanzhou@zju.edu.cn).

Conflicts of Interest: The authors declare no conflict of interest. The funders had no role in the design of the study; in the collection, analysis, or interpretation of data; in the writing of the manuscript; or in the decision to publish the results.

References

1. Duda, T.F.; Lynch, J.F.; Irish, J.D.; Beardsley, R.C.; Ramp, S.R.; Chiu, C.S.; Tang, T.Y.; Yang, Y.J. Internal tide and nonlinear internal wave behavior at the continental slope in the northern South China Sea. *IEEE J. Ocean. Eng.* **2004**, *29*, 105–130. [CrossRef]
2. Duda, T.F.; Rainville, L. Diurnal and semidiurnal internal tide energy flux at a continental slope in the South China Sea. *J. Geophys. Res.* **2008**, *113*, C03025. [CrossRef]
3. Cao, A.; Guo, Z.; Lv, X.; Song, J.; Zhang, J. Coherent and incoherent features, seasonal behaviors and spatial variations of internal tides in the northern South China Sea. *J. Mar. Syst.* **2017**, *172*, 75–83. [CrossRef]

4. Ray, R.D.; Zaron, E.D. Non-stationary internal tides observed with satellite altimetry. *Geophys. Res. Lett.* **2011**, *38*, L17609. [CrossRef]
5. Zhao, Z. Internal tide radiation from the Luzon Strait. *J. Geophys. Res. Oceans* **2014**, *119*, 5434–5448. [CrossRef]
6. Simmons, H.L.; Hallberg, R.W.; Arbic, B.K. Internal wave generation in a global baroclinic tide model. *Deep. Sea Res. Part II Top. Stud. Oceanogr.* **2004**, *51*, 3043–3068. [CrossRef]
7. Buijsman, M.C.; Klymak, J.; Legg, S.; Alford, M.H.; Farmer, D.; MacKinnon, J.A.; Nash, J.; Park, J.-H.; Pickering, A.; Simmons, H. Three-Dimensional Double-Ridge Internal Tide Resonance in Luzon Strait. *J. Phys. Oceanogr.* **2014**, *44*, 850–869. [CrossRef]
8. Xu, Z.; Liu, K.; Yin, B.; Zhao, Z.; Wang, Y.; Li, Q. Long-range propagation and associated variability of internal tides in the South China Sea. *J. Geophys. Res. Ocean.* **2016**, *121*, 8268–8286. [CrossRef]
9. Niwa, Y. Three-dimensional numerical simulation of M2internal tides in the East China Sea. *J. Geophys. Res. Space Phys.* **2004**, *109*, 04027. [CrossRef]
10. Jan, S.; Lien, R.C.; Ting, C.H. Numerical study of baroclinic tides in Luzon Strait. *J. Oceanogr.* **2008**, *64*, 789–802. [CrossRef]
11. Min, W.; Li, Q.; Zhang, P.; Xu, Z.; Yin, B. Generation and evolution of internal solitary waves in the southern Taiwan Strait. *Geophys. Astrophys. Fluid Dyn.* **2019**, *113*, 287–302. [CrossRef]
12. Zhao, Z. Southward Internal Tides in the Northeastern South China Sea. *J. Geophys. Res. Oceans* **2020**, *125*, 016554. [CrossRef]
13. Kelly, S.M.; Nash, J. Internal-tide generation and destruction by shoaling internal tides. *Geophys. Res. Lett.* **2010**, *37*, L23611. [CrossRef]
14. Nash, J.D.; Kelly, S.M.; Shroyer, E.L.; Moum, J.N.; Duda, T.F. The Unpredictable Nature of Internal Tides on Continental Shelves. *J. Phys. Oceanogr.* **2012**, *42*, 1981–2000. [CrossRef]
15. Gong, Y.; Rayson, M.D.; Jones, N.L.; Ivey, G.N. Directional decomposition of internal tides propagating from multiple generation sites. *Ocean Model.* **2021**, *162*, 101801. [CrossRef]
16. Marchesiello, P.; Nguyen, N.M.; Gratiot, N.; Loisel, H.; Anthony, E.J.; San Dinh, C.; Nguyen, T.; Almar, R.; Kestenare, E. Erosion of the coastal Mekong delta: Assessing natural against man induced processes. *Cont. Shelf Res.* **2019**, *181*, 72–89. [CrossRef]
17. Renault, L.; McWilliams, J.C.; Penven, P. Modulation of the Agulhas Current retroflection and leakage by oceanic current interaction with the atmosphere in coupled simulations. *J. Phys. Oceanogr.* **2017**, *47*, 2077–2100. [CrossRef]
18. Guo, Z.; Cao, A.; Lv, X.; Song, J. Impact of multiple tidal forcing on the simulation of the M2 internal tides in the northern South China Sea. *Ocean Dyn.* **2020**, *70*, 187–198. [CrossRef]
19. Large, W.G.; McWilliams, J.C.; Doney, S.C. Oceanic vertical mixing: A review and a model with a nonlocal boundary layer parameterization. *Rev. Geophys.* **1994**, *32*, 363–403. [CrossRef]
20. Amante, C.; Eakins, B.W. *ETOPO1 1 Arc-Minute Global Relief Model: Procedures, Data Sources and Analysis*; NOAA Technical Memorandum NESDIS NGDC-24; NOAA National Centers for Environmental Information: Silver Spring, MA, USA, 2009. [CrossRef]
21. Egbert, G.D.; Erofeeva, S.Y. Efficient inverse modeling of barotropic ocean tides. *J. Atmos. Ocean. Technol.* **2002**, *19*, 183–204. [CrossRef]
22. Kerry, C.G.; Powell, B.S.; Carter, G.S. Effects of Remote Generation Sites on Model Estimates of M2 Internal Tides in the Philippine Sea. *J. Phys. Oceanogr.* **2013**, *43*, 187–204. [CrossRef]
23. Kerry, C.G.; Powell, B.S.; Carter, G.S. The Impact of Subtidal Circulation on Internal Tide Generation and Propagation in the Philippine Sea. *J. Phys. Oceanogr.* **2014**, *44*, 1386–1405. [CrossRef]
24. Nash, J.; Alford, M.H.; Kunze, E. Estimating Internal Wave Energy Fluxes in the Ocean. *J. Atmos. Ocean. Technol.* **2005**, *22*, 1551–1570. [CrossRef]
25. Zilberman, N.V.; Merrifield, M.A.; Carter, G.S.; Luther, D.S.; Levine, M.D.; Boyd, T.J. Incoherent Nature of M2 Internal Tides at the Hawaiian Ridge. *J. Phys. Oceanogr.* **2011**, *41*, 2021–2036. [CrossRef]
26. Mercier, M.J.; Garnier, N.B.; Dauxois, T. Reflection and diffraction of internal waves analyzed with the Hilbert transform. *Phys. Fluids* **2008**, *20*, 86601. [CrossRef]
27. Peacock, T.; Mercier, M.J.; Didelle, H.; Viboud, S.; Dauxois, T. A laboratory study of low-mode internal tide scattering by finite-amplitude topography. *Phys. Fluids* **2009**, *21*, 121702. [CrossRef]
28. Bourget, B.; Dauxois, T.; Joubaud, S.; Odier, P. Experimental study of parametric subharmonic instability for internal plane waves. *J. Fluid Mech.* **2013**, *723*, 1–20. [CrossRef]
29. Wang, S.; Cao, A.; Chen, X.; Li, Q.; Song, J.; Meng, J. Estimation of the Reflection of Internal Tides on a Slope. *J. Ocean Univ. China* **2020**, *19*, 489–496. [CrossRef]
30. Wang, S.; Cao, A.; Li, Q.; Chen, X. Reflection of K 1 Internal Tides at the Continental Slope in the Northern South China Sea. *J. Geophys. Res. Oceans* **2021**, *126*, 017260. [CrossRef]
31. Cummins, P.F.; Oey, L.-Y. Simulation of Barotropic and Baroclinic Tides off Northern British Columbia. *J. Phys. Oceanogr.* **1997**, *27*, 762–781. [CrossRef]
32. Craig, W.; Guyenne, P.; Sulem, C. The surface signature of internal waves. *J. Fluid Mech.* **2012**, *710*, 277–303. [CrossRef]
33. Alford, M.H.; MacKinnon, J.A.; Nash, J.; Simmons, H.; Pickering, A.; Klymak, J.; Pinkel, R.; Sun, O.; Rainville, L.; Musgrave, R.; et al. Energy Flux and Dissipation in Luzon Strait: Two Tales of Two Ridges. *J. Phys. Oceanogr.* **2011**, *41*, 2211–2222. [CrossRef]
34. Wang, Y.; Xu, Z.; Yin, B.; Hou, Y.; Chang, H. Long-Range Radiation and Interference Pattern of Multisource M 2 Internal Tides in the Philippine Sea. *J. Geophys. Res. Oceans* **2018**, *123*, 5091–5112. [CrossRef]